Journal of Magnetism and Magnetic Materials 528 (2021) 167700

Contents lists available at ScienceDirect

Journal of Magnetism and Magnetic Materials

journal homepage: www.elsevier.com/locate/jmmm

Topological Hall effect in magnetic topological insulator films

Jian-Xiao Zhang [a], Domenico Andreoli [b], Jiadong Zang [b], Chao-Xing Liu [a,*]

[a] Department of Physics, The Pennsylvania State University, University Park, Pennsylvania 16802-6300, USA
[b] Department of Physics, University of New Hampshire, Durham, New Hampshire 03824, USA

ARTICLE INFO

Keywords:
Skyrmion
Topological Hall effect
Spin–orbit coupling

ABSTRACT

Geometric Berry phase can be induced either by spin–orbit coupling, giving rise to the anomalous Hall effect in ferromagnetic materials, or by chiral spin texture, such as skyrmions, leading to the topological Hall effect. Recent experiments have revealed that both phenomena can occur in topological insulator films with magnetic doping, thus providing us with an intriguing platform to study the interplay between these two phenomena. In this work, we report on a numerical simulation of the anomalous Hall and topological Hall effects in a four-band model that can properly describe the quantum well states in the magnetic topological insulator films by combining Landauer–Büttiker formula and the iterative Green's function method. Our numerical results suggest that spin–orbit coupling in this model plays a different role in the quantum transport in the clean and disordered limits. In the clean limit, spin–orbit coupling mainly influences the longitudinal transport but does not have much effect on topological Hall conductance. In the disordered limit, the longitudinal transport is determined by disorder scattering and spin–orbit coupling is found to affect strongly the topological Hall conductance. This sharp contrast unveils a dramatic interplay between spin–orbit coupling and disorder effect in topological Hall effect in magnetic topological insulator systems.

1. Introduction

For electric conductors placed in an external magnetic field, the Lorentz field felt by electrons can lead to a voltage transverse to the electric current, which is known as the Hall effect [1]. In magnetic systems, the exchange interaction between electron spin and magnetic moments can give rise to additional topological contributions to the Hall effect. In a ferromagnetic (FM) system with a strong spin–orbit coupling (SOC), the additional Hall contribution is induced by Berry phases accumulated by the adiabatic motion of quasiparticle on the Fermi surface in the momentum space and normally known as (intrinsic) anomalous Hall effect (AHE) [2,3]. Although AHE can also be induced by other scattering mechanism (known as extrinsic AHE) [2], we only consider the intrinsic origin of the AHE in this study. On the other hand, when electrons propagate through chiral magnetic structures, e.g. skyrmions, in the real space, they can also feel Berry phase due to the magnetization texture, leading to the so-called "topological Hall effect (THE)" (also known as "geometric Hall effect") [4–8]. Both Hall phenomena originate from Berry phase contribution and thus are topological. An intriguing question is how to understand the topological contribution to the Hall effect in a magnetic skyrmion system with strong SOC, where the Berry phase exists in both the real and momentum spaces.

Topological insulator (TI) films with magnetic doping, dubbed "magnetic topological insulator (MTI)" below, provide an ideal platform to explore the interplay between AHE and THE. The coexistence of strong SOC and ferromagnetism in MTI films can result in a strong AHE [9], and the Hall resistance can even achieve the quantized value when the chemical potential is tuned into the magnetization gap of surface states. Such phenomenon, known as the quantum anomalous Hall (QAH) effect [10–13], has been experimentally observed in Cr or V doped $(Bi,Sb)_2Te_3$ilms [14]. Furthermore, the surface states in TI film can also mediate Dzyaloshinsky–Moriya (DM) interaction between magnetic moments due to spin-momentum locking [15,16]. As a result, chiral magnetic structures, such as skyrmion, are also possible. Indeed, recent experiments on Cr-doped-$(Bi,Sb)_2Te_3$/$(Bi,Sb)_2Te_3$ structure [17] and Mn-doped Bi_2Te_3 [18] have observed a hump in the Hall resistance hysteresis loop at a small magnetic field. The hump structure is attributed to THE while the Hall hysteresis loop implies AHE. Furthermore, the concurrence of QAH effect and THE has been demonstrated in MTI sandwich structure [19]. Therefore, the interplay between the AHE from ferromagnetism and the THE from magnetic skyrmion will be

* Corresponding author.
E-mail address: cxl56@psu.edu (C.-X. Liu).

https://doi.org/10.1016/j.jmmm.2020.167700
Received 28 July 2020; Received in revised form 19 November 2020; Accepted 23 November 2020
Available online 23 January 2021
0304-8853/© 2021 Elsevier B.V. All rights reserved.

substantial to understand the electron transport phenomena in MTI films. In addition, MTI is normally highly disordered due to magnetic doping and it is not well understood how the disorder influences the THE in such strong spin–orbit coupled materials.

In this work, we report on the numerical study on the magneto-transport of MTI films with a magnetic skyrmion based on a four-band model by combining the iterative Green's function method and the Landauer–Buttiker formalism. Our numerical results suggest that (1) both AHE and THE can coexist in our model system and the total Hall effect can be decomposed into the summation of these two effects in the metallic and adiabatic regime; (2) in the clean limit, the topological Hall conductance (THC) almost remains constant but the topological Hall resistance (THR) can increase due to the reduction of longitudinal conductance when the SOC is increasing; (3) in the disorder limit, both the THC and THR are increasing with increasing SOC, while longitudinal conductance is not influenced much by SOC.

Our results are organized as the following. In Section 2, we will describe our model Hamiltonian for the quantum well states in MTI films. In Section 3, we will simulate magneto-transport in MTI films based on Landauer–Buttiker formalism for the model Hamiltonian and analyze the numerical results. The disorder effect is numerically calculated and discussed in Section 4. The implication of our numerical results and the conclusion will be discussed in Section 5.

2. Model Hamiltonian

The TI films can be modeled by a 3D four-band model in a quantum well (QW) with an infinite potential along the z direction [20,21]. The confinement effect along the z direction can be approximated by choosing $\langle k_z\rangle = 0$ and $\langle k_z^2\rangle = (n_b\pi/d)^2$, where n_b is an integer to label the sub-band index and d is the width of the QW [22]. As shown in the Appendix A [23], we project the 3D four-band model into the subspace spanned by these QW sub-bands and obtain a 2D four-band BHZ-like model given by [20,21]

$$H_0(\boldsymbol{k}) = M(\boldsymbol{k})\sigma_0\tau_z + \alpha(k_y\sigma_x - k_x\sigma_y)\tau_x \tag{1}$$

on the basis $\{|+\uparrow\rangle,|+\downarrow\rangle,|-\uparrow\rangle,|-\downarrow\rangle\}$, where σ and τ are Pauli matrices for spin and orbital subspaces. $M(\boldsymbol{k}) = M_0 + B(k_x^2 + k_y^2)$ and α labels the SOC strength. The parameter $M_0 = M + B_1(n_b\pi/d)^2$ (See appendix for details) depends on the integer sub-band index n_b. Depending on the sub-band index n_b (assuming $M < 0$ and $B_1 > 0$), the four band model for the QW sub-bands can be in the inverted regime if $M_0B < 0$ or in the normal regime $M_0B > 0$.

It should be mentioned that the Hamiltonian (1) is block-diagonal with one block set by the basis $\{|+\uparrow\rangle,|-\downarrow\rangle\}$ and the other block by the basis $\{|+\downarrow\rangle,|-\uparrow\rangle\}$. These two blocks are related to each other by time-reversal symmetry and are degenerate. This degeneracy will be broken when introducing ferromagnetism or magnetic skyrmion into the system. Since we focus on the transport regime dominated by these QW states in this work, we expect that multiple QW sub-bands with different n_b will be present at the Fermi energy. To simplify the problem, we treat QW sub-bands in the Hamiltonian (Eq. (1)) with different n_b independently. Thus, we may choose M_0 as an independent parameter and discuss below the transport behaviors for the parameter M_0 in different regimes. The SOC term (α term) couples the state $|+\uparrow\rangle$ ($|+\downarrow\rangle$) to the state $|-\downarrow\rangle$ ($|-\uparrow\rangle$) in different orbital basis, which is different from the conventional Rashba SOC where the SOC term couples different spin states in the same orbital basis.

For MTI, the exchange interaction between electron spin and magnetic moment is given by

$$H_{\rm ex}(x,y) = \boldsymbol{m}(x,y)\cdot\boldsymbol{\sigma}\tau_0, \tag{2}$$

where $\boldsymbol{m}(x,y)$ represents the magnetization. The specific representation of Pauli Matrices is due to the choice of basis in Eq. (1), which is equivalent to the more standard Hamiltonian form [21] up to a unitary transformation. The magnetic skyrmion texture can be taken into account by choosing the $\boldsymbol{m}$ configuration.

$$\begin{aligned}\boldsymbol{m} &= m_0\{\sin\theta\cos\phi, \sin\theta\sin\phi, \cos\theta\}\\ \theta &= \pi\tanh\left(\frac{\rho}{R}\right)\\ \phi &= n\varphi + \eta,\end{aligned} \tag{3}$$

where m_0 represents the magnetization strength, θ and ϕ label the magnetization direction, ρ and φ define the spatial polar coordinates with $(x,y) = (\rho\cos\varphi, \rho\sin\varphi)$, and R is the radius of the skyrmion. The chirality of the skyrmion is characterized by the integer number n, which is chosen to be $+1$ (a single skyrmion) or -1 (a single anti-skyrmion) below. The parameter η denotes the helicity of the skyrmion. The dependence of the Hall signal on the skyrmion helicity [24,25] is discussed in Appendix E [23] and turns out to be not essential for qualitative behaviors discussed below, so our numerical results mainly focus on skyrmion chirality.

Physically, magnetic skyrmion can be energetically stabilized by the interplay of exchange coupling and DM interaction [26], and only skyrmion with chirality $+1$ is expected in the MTI film [17,18]. In this study, we focus on the magneto-transport property induced by the chiral structure of skyrmions. For convenience to study the chirality influence on Hall transport, we will evaluate the Hall conductance and resistance in both skyrmion and anti-skyrmion configurations without considering their energetic stability. This calculation allows us to theoretically extract the chirality-dependent and independent parts of Hall transport.

Due to the absence of translation symmetry in a system with a single skyrmion, we numerically explore magneto-transport directly in the real space. To perform such calculation, we implement the tight-binding regularization on the Hamiltonian (1) and (2), which is given by

$$\widehat{H} = \widehat{H}_0 + \sum_i \Psi_i^\dagger H_{\rm ex}\Psi_i,\ \widehat{H}_0 = \sum_i \Psi_i^\dagger \epsilon_i \Psi_i + \sum_{\langle i,j\rangle}(V_{ij}\Psi_j^\dagger\Psi_i + \text{h.c.}), \tag{4}$$

where $\Psi_i^\dagger$ presents $(c_{i,+\uparrow}^\dagger, c_{i,+\downarrow}^\dagger, c_{i,-\uparrow}^\dagger, c_{i,-\downarrow}^\dagger)$ at the position $i = (i_x, i_y)$. ϵ_i is the on-site energy and V_{ij} is the hopping matrix between the nearest neighbors i and j. Both ϵ_i and V_{ij} are 4 by 4 matrices and their detailed forms can be related to those in the continuous model (Eq. (1)), as listed in the Appendix B [23]. The consistency between the tight-binding Hamiltonian (4) and the continuous Hamiltonian (1) and (2) is also discussed in the Appendix B [23].

We consider a 2D square lattice with the side length L. The skyrmion texture is located at the center of the lattice, as shown in Fig. 1(a). Four semi-infinite leads with the width L, labeled as 1 to 4 in Fig. 1, are attached to each side of the square lattice. We adopt the recursive Green's function method [27] to evaluate the transmission coefficient T_{pq} between the leads p and q ($p,q = 1,2,3,4$). The relationship between currents and voltages is calculated using the Landauer–Büttiker

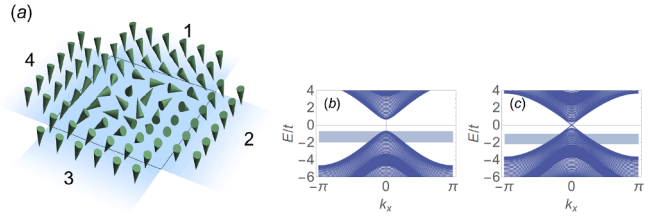


Fig. 1. (a) Schematic configuration of the system. The square region in the center represents the sample, and the extended transparent edges represent semi-infinite FM leads. A skyrmion of $m = 1, \eta = \pi/2, R = 0.4L$ is shown at the origin. Cones point to the local magnetic moment direction. (b, c) Band dispersions for the Hamiltonian Eq. (4) for two parameter sets (i) and (ii) (see main text). A periodic boundary condition is applied on the y direction. The shaded regions show the energy range for the transport calculations in Fig. 2–4.

formalism

$$I_p = e^2 \Big/ h \sum_{q \neq p} (T_{qp} V_p - T_{pq} V_q). \tag{5}$$

Due to the charge conservation of the whole system, the matrix T is singular. Without loss of generality, we set $V_4 = 0$ and remove the corresponding column/row in T. To set up a Hall configuration, we consider a current flow from the lead 1 to 3, as setting $I_1 = -I_3 = I$ and $I_2 = 0$. Voltages of the leads are calculated through $(V_1, V_2, V_3)^{\intercal} = \frac{h}{e^2} T^{-1} (I_1, I_2, I_3)^{\intercal}$, where the matrix T is the 3×3 transmission matrix. The longitudinal resistance R_{xx} and the Hall resistance R_{xy} can be extracted by $R_{xx} = (V_1 - V_3)/I$ and $R_{xy} = V_2/I$.

3. Numerical results and analysis in the clean limit

Fig. 2(a1) and (b1) reveal the Hall resistance as a function of the Fermi energy in different parameter regimes. Here we choose a system of length $L = 80a_0$ and Skyrmion radius $R = 0.4L$. Hopping parameters are expressed in term of the nearest-neighbor hopping strength $t \equiv B/a_0^2$ (See Appendix B [23]).

We consider two sets of parameters, one for the trivial regime, denoted as (i), and the other for the QAH regime, denoted as (ii) below. While all the other parameters are the same ($m_0 = 4/3, \alpha/t = 2, a_0 = 1, B = 1$) for the parameter sets (i) and (ii), the parameter M_0 is chosen to be different ($M_0 = 2$ for (i) and $M_0 = 1$ for (ii)). To see the topological property of the full Hamiltonian with these two parameter sets, we may consider the FM case with $\boldsymbol{m}(x,y) = m_0(0,0,1)$. For the parameter set (i), we notice that both blocks of bands in the Hamiltonian (4) are in the normal regime since $(M_0 \pm m_0)B > 0$. In contrast, the system for the parameter set (ii) is in the QAH regime since one block is in the normal regime $(M_0 + m_0)B > 0$ while the other is in the inverted regime $(M_0 - m_0)B < 0$. The corresponding energy dispersions for a slab configuration with these two parameter sets are shown in Fig. 1(b) and (c), from which one can see a full gap for the parameter set (i) and gapless chiral edge states appear in the bulk gap for the parameter set (ii). It should be emphasized that for either parameter sets, we can estimate the adiabatic parameter as $\lambda = m_0\tau/\hbar = 2m_0R/\hbar v_F = 1.33t \cdot 48a/2at \approx 32$, where τ is the time-of-flight of an electron passing through the textured region, v_f is the Fermi velocity which is estimated through the slope of the band structure within the energy range. According to the value of λ, our numerical simulations belong to the adiabatic region.

In this work, we focus on the transport behavior of the metallic regime when the Fermi energy E_f crosses one valence band top ($E_f/t \in [-2, -0.7]$ for the parameter set (i) and $[-2.6, -1]$ for the parameter set (ii) in Fig. 1(b) and (c)). For the purpose of the quantized conductance within the gap, the parameter set (i) and (ii) represent a comparison between a trivial and a non-trivial gap.

In the transport calculation, three magnetic configurations, namely ferromagnetism ($\hat{m} = -m_0\hat{z}$), a skyrmion ($n = +1$) and an anti-skyrmion ($n = -1$) are considered and the corresponding Hall resistances R_{FM}, $R_{\mathrm{Sk},+1}$ and $R_{\mathrm{Sk},-1}$ are shown by the yellow, red and blue lines in Fig. 2(a1) and (b1) for the parameter sets (i) and (ii), respectively. One can clearly see that $R_{\mathrm{Sk},+1}$ is much larger than R_{FM}, while $R_{\mathrm{Sk},-1}$ has the opposite sign. For the FM case, the Hall resistance only originates from the AHE, while in the skyrmion cases, both THE and AHE can contribute due to the coexistence of strong SOC and chiral magnetic structure. We expect the THE (AHE) is dependent (independent) on the chirality of the skyrmions. For the convenience of the discussion below, we decompose the Hall resistance $R_{\mathrm{Sk},\pm1}$ into chirality-dependent and independent parts, and *defines* the former part as R_{THE} and the latter part as R_{AHE},

$$R_{\mathrm{Sk},n} = R_{\mathrm{AHE}} + nR_{\mathrm{THE}}, \tag{6}$$

where the index n stands for the chirality of the skyrmion. As pointed out in the previous section, the above decomposition neglects the influence of helicity.

Based on the decomposition of Eq. (6), Fig. 2(a2) and (b2) depict R_{AHE} (blue line) and R_{THE} (yellow line) as a function of Fermi energy for the parameter sets (i) and (ii), respectively. In addition, R_{FM} is shown by the red line. Fig. 2(a2) and (b2) show the following features. (1) R_{FM} generally shows a similar behavior as the blue line of R_{AHE} (except that the Fermi energy is close to band gap), and thus the magnetic skyrmion does not have a strong influence on the AHE in the metallic regime and validates the decomposition of the Hall resistance. (2) R_{AHE} is much larger for the parameter set (i) than that for (ii), due to the energy range (shaded area in Fig. 1(b,c)) is closer to band center for parameter set (ii). (3) For both parameter sets, we notice that R_{THE} increases rapidly when the Fermi energy is tuned towards the valence band top.

We next turn to the Hall conductance with the same parameters, as shown in Fig. 3. Here the red, blue and yellow lines are for the Hall conductance with the FM, skyrmion ($n = +1$) and anti-skyrmion ($n = -1$) configurations in Fig. 3(a1) and (b1) for two parameter sets. A similar decomposition

$$G_{\mathrm{Sk},n} = G_{\mathrm{AHE}} + nG_{\mathrm{THE}} \tag{7}$$

is considered and the corresponding G_{AHE} and G_{THE} are plotted in Fig. 3 (a2) and (b2), which show the following features. (1) The decomposition of Hall conductance also remains valid in most energy ranges, as indicated by the coincidence between G_{AHE} and G_{FM} in most energy ranges. (2) In contrast to Hall resistance, the Hall conductance is almost a constant in the whole metallic region for both parameter sets. (3) G_{AHE} (or G_{FM}) is smaller for the parameter set (i) compared to that for (ii) while G_{THE} is comparable for both parameter sets. Fig. 4(a) and (b) ((c) and (d)) reveal the THE contribution R_{THE} (G_{THE}) from the decomposition of Eq. (6) (Eq. (7)) as a function of the Fermi energy for different SOC strength α for both parameter sets. An enhancement of R_{THE} is found while G_{THE} remains almost unchanged when increasing the SOC strength or the Fermi energy for both parameter sets. G_{THE} is only found to drop when the Fermi energy is close to the band gap (insulating regime).

The above numerical calculation focuses on the valence band and we

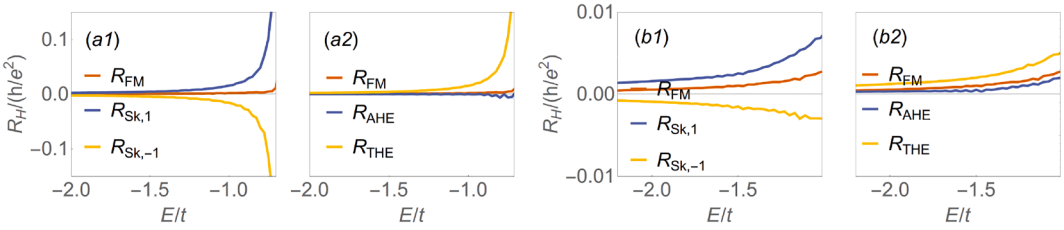


Fig. 2. (a1, b1) Red, blue and yellow lines represent Hall resistance in FM, skyrmion and anti-skyrmion cases as the function of Fermi energy, for the parameter sets (i) and (ii), respectively. SOC strength $\alpha/t = 2$. (a2, b2) Blue and yellow lines are the extracted AHE and THE contribution R_{AHE} and R_{THE} from Eq. (6). Red lines are the same in (a1, b1) representing the FM contribution R_{FH} as a comparison. Note that R_{AHE} and R_{FH} are close in value in a wide range of energy, suggesting the skyrmion texture has a minimum reduction on the AHE effect.

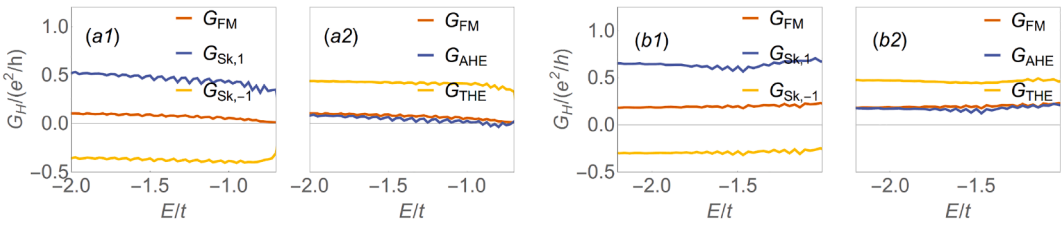


Fig. 3. The same system as Fig. 2 expressed in conductances. (a1, b1) the Hall conductances for the parameter sets (i) and (ii), respectively. (a2, b2) the extracted decomposition into AHE and THE contribution. The ferromagnetic system is marked with red lines. Note that G_{FM} is also close to G_{AHE}, showing that the decomposition approximation works for both resistance and conductance.

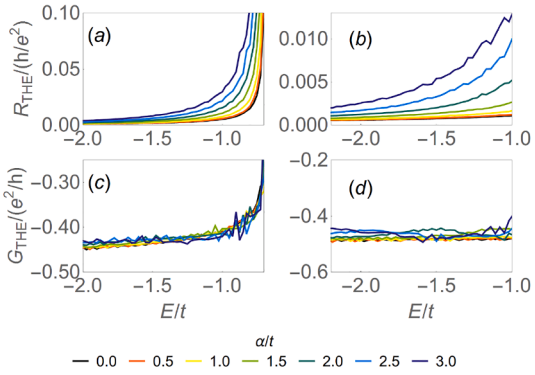


Fig. 4. (a) and (b) show THR R_{THE} as the function of Fermi energy and SOC strength α, for the parameter sets (i) and (ii), respectively. (c) and (d) show THC G_{THE} decomposed in the similar way.

next briefly mention the transport behavior of the conductance bands. For the SOC = 0 case, the valence and conduction bands are completely symmetric, and the corresponding R_{THE} are an even function as a function of energy about the gap center. With SOC, the conductance behaviors in valence band top and conduction band bottom will have some quantitative difference due to different spin textures, but the qualitative behaviors are the same, as shown in Appendix Fig. D.2.

To understand our numerical results, we will next present a theoretical analysis of the transport behavior of the model based on our numerical simulation of the Landauer–Büttiker formalism. The symmetry property of the transmission matrix T_{pq} in the Eq. (5) will be first analyzed. For the FM and $n = +1$ skyrmion cases, the system respects the C_4 rotation symmetry, while for the anti-skyrmion with $n = -1$, the system possesses the S_4 improper rotation symmetry. In all cases, we find the transmission matrix elements can be characterized by three independent parameters based on the following relations

$$\begin{aligned} T_{13} &= T_{24} = T_{31} = T_{42} \equiv -a \\ T_{14} &= T_{21} = T_{32} = T_{43} \equiv -b \\ T_{12} &= T_{23} = T_{34} = T_{41} \equiv -c \end{aligned} \tag{8}$$

where a, b and c can be understood as the probability of electronic modes going straight, turning left and turning right, respectively, after they entered the spin-textured structure from any of the leads. With this simplification, direct calculations from the Landauer–Büttiker formalism give rise to the Hall and longitudinal resistance as

$$\begin{aligned} R_{xy} &= \frac{(b-c)}{2a^2 + 2a(b+c) + b^2 + c^2} \approx \frac{b-c}{2(a+b)^2} \equiv \frac{\Delta}{2\beta^2} \\ R_{xx} &= \frac{(2a+b+c)}{2a^2 + 2a(b+c) + b^2 + c^2} \approx \frac{1}{a+b} \equiv \frac{1}{\beta}, \end{aligned} \tag{9}$$

where we define the parameters $\beta \equiv a+b$ to be the transmission probability and $\Delta \equiv (b-c)$ to be the asymmetric scattering between the left and right directions. We further assume $\Delta \ll b \approx c$, which can be justified based on our numerical calculations for both parameter sets. The corresponding Hall and longitudinal conductance is

$$\begin{aligned} G_{xy} &\approx -\Delta/2 \\ G_{xx} &\approx \beta. \end{aligned} \tag{10}$$

Eq. (9) and (10) are the basis for the analysis below. We can see that β is related to the forward transmission and determines the longitudinal conductance G_{xx} while Δ represents the asymmetry between the left and right scattering and determines the Hall conductance G_{xy}. In Fig. 5, we demonstrate the behaviors of β and Δ for the parameter set (i) as an example, from which we can understand the behaviors of AHE and THE.

Below we will analyze the behavior of Δ first (Fig. 5(d)–(f)). In Fig. 5 (d), one can see that Δ increases when increasing the SOC parameter α in the FM case. From Fig. 5(e) and (f), we find the value of Δ is much larger when there is a skyrmion or anti-skyrmion as compared to the FM case. We may also consider a decomposition $\Delta_{Sk,n} = \Delta_{AHE} + n\Delta_{THE}$ and the corresponding Δ_{THE} and Δ_{AHE} are plotted in Fig. 6(a) and (b), respectively. One can see that all the curves for Δ_{THE} fall into one line and thus are independent of the SOC parameter α, while Δ_{AHE} increases rapidly with α. From Eq. (10), we expect that G_{xy} exhibits a similar behavior as Δ, which was indeed revealed in Fig. 4(c). Therefore, we conclude that SOC mainly increases the AHE contribution, but has little influence on the THE contribution to our four-band model in the clean limit.

Next, let us analyze the behavior of transmission β. For all three spin textures, the values of β and the dependence of β on SOC and the Fermi energy are quite similar, and thus we would not specify the magnetic texture for the discussion below. As expected, β is decreasing when tuning Fermi energy to the valence band top (more insulating). In addition, we find a rapid decreasing of β when increasing the SOC parameter α in Fig. 5. This can be understood as the following. SOC tends to induce precession of electron spin and rotate it from the easy axis set by local magnetization. As a consequence, a strong scattering can be induced by the exchange coupling between electron spin and magnetic

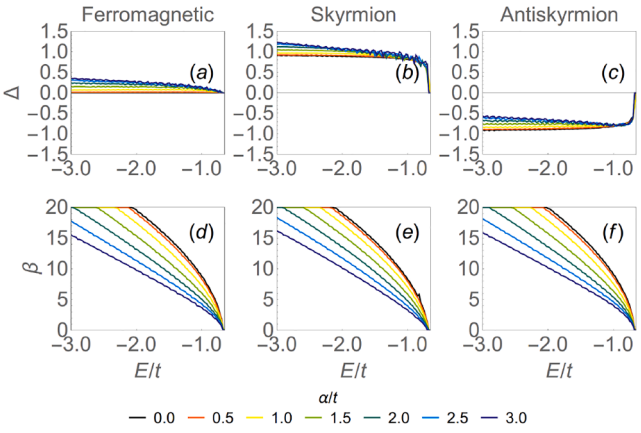


Fig. 5. (a), (b) and (c) show Δ as a function of E for FM, skyrmion and anti-skyrmion cases. (d), (e) and (f) reveal the energy dependence of β for FM, skyrmion and antiskyrmion cases. Here we consider the parameter set (i).

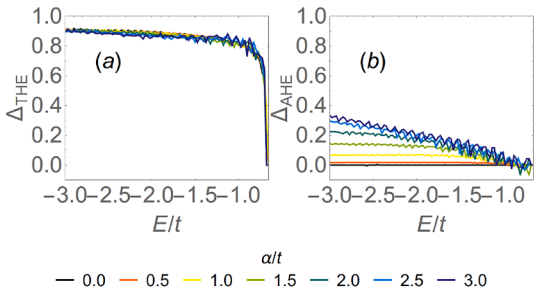


Fig. 6. (a) and (b) show the decomposition of Δ into the THE (Δ_{THE}) and AHE part (Δ_{AHE}), respectively. Here we choose the parameter set (i).

moments, and thus reduces transmission. It turns out that the reduction of transmission β has a substantial influence on the behavior of Hall resistance R_{xy}. From Eq. (9), we can see that R_{xy} depends on the ratio between Δ and β^2. Therefore, although increasing SOC does not enhance Δ, it reduces β, and thus increases R_{xy} as shown in Fig. 4. (For a full figure of R_{xy} for all SOC and spin textures, please see Appendix Fig. C1.) This analysis leads to the conclusion that the behavior of R_{THE} is mainly determined by the forward transmission β, rather than the asymmetric scattering Δ for our model in the clean limit.

4. Disorder effect

We next examine the disorder effect on THE in MTI films, as shown in Fig. 8(a–d), which reveal new features compared to Fig. 4 in the clean limit. To consider the disorder effect, we introduce a spin-independent uniformly-distributed random on-site potential term $H_d = \sum_i \Psi_i^\dagger V_{d,i} \Psi_i$ where $V_{d,i} = \mathrm{Diag}(\mathscr{V}_+, \mathscr{V}_+, \mathscr{V}_-, \mathscr{V}_-)$ and $\mathscr{V}_\pm \in [-V_{imp}/2, V_{imp}/2]$ with $0 < V_{imp} \leqslant 2t$ chosen in our calculations.

We set up a separate simulation to reveal the relation between the disorder strength, expressed in unit of hopping energy, versus the mean free path λ of the system. We follow the process described in Ref. [24] by setting up a two-terminal measurement of a ribbon configuration with width $w = 80a_0$ and different length l. The Hamiltonian of the system is set to be the same as the ferromagnetic system used in transport measurement, with on-site disorder as above. The conductance G decays as a function of l, as shown in Fig. 7, which follows the semiclassical formula $G = G_0/(1 + \frac{l}{\lambda})$, where G_0 is the unimpeded conductance. The extracted mean free path is dependent on the energy E and the parameters α and M. Here we present several typical values of λ as a function of disorder strength V_{imp}, where the parameters fall in the range of our transport calculation as an illustration. The resulted mean free path λ ranges from 50 to 300 a_0, which is large compared with the skyrmion size, and thus our system is still between ballistic and diffusive transport regimes.

All the calculations are performed with the disorder average over 160 samples. After such a sample average, the uncertainty (dictated by the error bars in Fig. 4) is much smaller than its mean value. We implement a similar decomposition of Hall conductance and resistance,

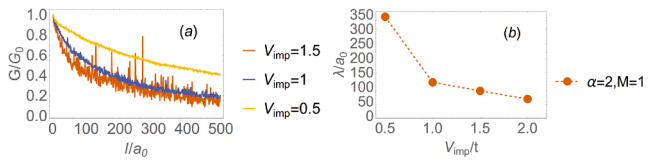


Fig. 7. (a) Relative conductance for a ferromagnetic ribbon system as a function of transmission length l, for different disorder strength. For this figure, $\alpha = 2, M = 1, E = -2$ is chosen for illustration. (b) Mean free path λ/a_0 extracted from the relative conductance, for the same value of $\alpha = 2, M = 1, E = -2$. Within the range of disorder strength, the mean free path is roughly on the order of 100. As disorder strength increases, the mean free path decreases rapidly, but is still large compared to the skyrmion size.

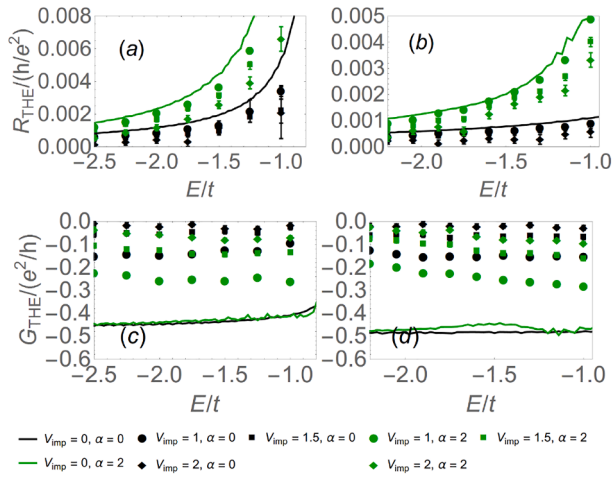


Fig. 8. (a) and (c) reveal R_{THE} and G_{THE} for the parameter set (i) under different disorder strength ($V_{imp} = 0, 1, 1.5, 2$ in unit of t), respectively. Green and black colors represent $\alpha/t = 2$ and 0 cases, respectively. (b) and (d) are the same as (a) (c), except that we choose the parameter set (ii).

as specified in Eq. (6) and (7) for each individual run, and the disorder-averaged Hall resistance (R_{THE}) and conductance (G_{THE}) from the THE contribution are revealed in Fig. 8 for two parameter sets (i) and (ii), respectively. Here the circle, square and diamond label different disorder strength $V_{imp} = 1, 1.5$ and 2 in the unit of t, while the green and black colors are for different SOC strength ($\alpha/t = 0$ and $\alpha/t = 2$). The solid lines show the results in the clean limit for comparison. With increasing the disorder strength, one can clearly see the decreasing of both Hall resistance R_{THE} and conductance G_{THE}. A striking feature emerges in the Hall conductance G_{THE} when increasing disorder strength. G_{THE} is unchanged for different SOC strength in the clean limit, as seen by the coincidence between black and green solid lines in Fig. 8(c) and (d). In contrast, for intermediate or strong disorder strength, G_{THE} at a large SOC $\alpha/t = 2$ can be much larger than that at zero SOC, as shown by the green and black markers in Fig. 8(c) and (d). This suggests that SOC can stabilize the THE against disorder scattering. We also analyze the disorder-averaged forward transmission β and asymmetric scattering Δ, shown in Fig. 9(a) and (b). Interestingly, we find that with increasing disorder scattering, forward transmission β, although being reduced for both SOC strengths, becomes comparable for $\alpha/t = 0$ and $\alpha/t = 2$ when V_{imp} is increased above $1.5t$. This suggests that the mean-free path of electrons is determined by disorder, rather than SOC, at this disorder strength $V_{imp}/t = 2$. In contrast, although the asymmetric scattering parameter Δ is reduced for both SOC strengths, its reduction is much slower when the SOC α is strong, which can be clearly seen by the fact that the green markers ($\alpha/t = 2$) are above the black markers ($\alpha/t = 0$) in Fig. 9(b). In contrast to the clean limit, in which SOC only enhances

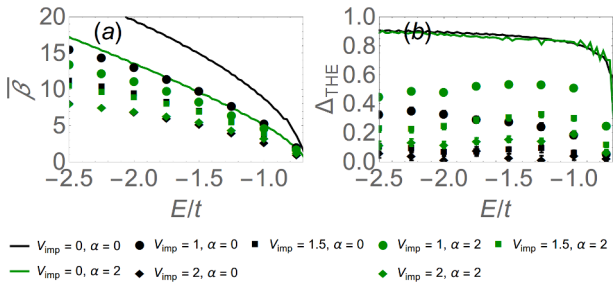


Fig. 9. (a) and (b) reveal $\bar{\beta}$ and Δ_{THE} as a function of E in both disordered and clean limit. Here the colors represent different SOC strengths (green for $\alpha/t = 2$ and black for $\alpha/t = 0$), and the line, circle, square and diamond represent $V_{imp} = 0, 1, 1.5, 2$, respectively.

R_{xy} but not G_{xy} due to the reduction of transmission β, SOC mainly influences the asymmetric scattering Δ and thus will enhance both R_{xy} and G_{xy} in the disordered limit. Therefore, we conclude that the THE is stabilized by SOC in the disordered limit.

5. Discussion and conclusion

Our work has numerically studied the AHE and THE in an MTI model with skyrmion configuration and revealed the intricate magneto-transport behaviors due to the interplay between SOC, magnetic texture and disorders. In the adiabatic regime, the magnetic texture can be analytically transformed to an emergent gauge field by neglecting spin-flip process and physically the electron spin follows the magnetization direction of magnetic texture and experiences a Berry curvature [28]. However, the existence of SOC will compete with the emergent gauge field and may induce the spin-flip process. Thus, the analytical method to attack this problem is challenging and requires further consideration. Our numerical simulations suggest that the spin scattering induced by SOC can back-scatter the electrons, but will not affect much the asymmetric scattering Δ, at least in the parameter regime considered here. Disorder effect will normally reduce THE, as shown in Ref. [24]. Our numerical results also reveal that SOC can reduce the disorder scattering and thus stabilize the THE. A more analytical method (such as the Boltzman equation and diagram expansion calculation [2]) is called for to provide a theoretical understanding of these numerical results. It should be pointed out that the SOC term we used here preserves inversion symmetry and thus is different from the Rashba SOC, which breaks inversion symmetry and responses for DM interaction. Including Rashba SOC in the calculation may bring new features and will require further studies, which is beyond the scope of the current work. Given the recent experimental efforts in MTI systems [17,18], our numerical results will provide a guidance to understand these magneto-transport measurements and may stimulate further experimental studies. We would like to point out that although the current calculation is on a specific skyrmion texture, the presence of transverse scattering should exist for any spin textures, including random state, with net chirality [29]. It will be interesting to generalize this work to the investigation of THE-AHE crossover in other chiral systems. It is also interesting to investigate the spin Hall effect in this system. In the SOC free case ($\alpha = 0$), the topological spin Hall effect has been reported [30] when the Fermi surface lies between $t \pm J_H$, where t is the hopping parameter, and J_H in analogy to our m_0 is the exchange coupling between conduction electrons and local magnetic moments. In our model, the SOC α plays an important role. In the small m_0 limit, quantum spin Hall effect from the band origin is dominant. At large m_0 limit, the conduction spins are fully polarized by local moments, and only one species of spin is relevant so that the spin Hall effect is absent. The topological spin Hall effect might take place at moderate exchange m_0 value, and its interplay with the SOC-induced quantum spin Hall effect is an interesting question worthy future investigations.

CRediT authorship contribution statement

Jian-Xiao Zhang: Methodology, Software, Data curation, Writing - original draft. **Domenico Andreoli:** Formal analysis. **Jiadong Zang:** Formal analysis, Writing - review & editing, Funding acquisition. **Chao-Xing Liu:** Conceptualization, Methodology, Writing - review & editing, Supervision, Funding acquisition.

Declaration of Competing Interest

The authors declare that they have no known competing financial interests or personal relationships that could have appeared to influence the work reported in this paper.

Acknowledgement

We acknowledge the discussion with C.Z. Chang and M.H.W. Chan. Work (numerical simulation and the analysis of numerical results) at Penn State is primarily supported by the DOE grant (DE-SC0019064). Work at UNH was supported by the U.S. Department of Energy (DOE), Office of Science, Basic Energy Sciences (BES) under Award No. DE-SC0016424.

Appendix A. Supplementary data

Supplementary data associated with this article can be found, in the online version, at https://doi.org/10.1016/j.jmmm.2020.167700.

References

[1] E.H. Hall, On a new action of the magnet on electric currents, American Journal of Mathematics 2 (3) (1879) 287–292.
[2] N. Nagaosa, J. Sinova, S. Onoda, A. MacDonald, N. Ong, Anomalous hall effect, Reviews of Modern Physics 82 (2) (2010) 1539.
[3] R. Karplus, J. Luttinger, Hall effect in ferromagnetics, Physical Review 95 (5) (1954) 1154.
[4] Y. Machida, S. Nakatsuji, Y. Maeno, T. Tayama, T. Sakakibara, S. Onoda, Unconventional anomalous hall effect enhanced by a noncoplanar spin texture in the frustrated kondo lattice pr 2 ir 2 o 7, Physical Review Letters 98 (5) (2007), 057203.
[5] N. Kanazawa, M. Kubota, A. Tsukazaki, Y. Kozuka, K. Takahashi, M. Kawasaki, M. Ichikawa, F. Kagawa, Y. Tokura, Discretized topological hall effect emerging from skyrmions in constricted geometry, Physical Review B 91 (4) (2015), 041122.
[6] A. Neubauer, C. Pfleiderer, B. Binz, A. Rosch, R. Ritz, P. Niklowitz, P. Böni, Topological hall effect in the a phase of mnsi, Physical Review Letters 102 (18) (2009), 186602.
[7] L. Oveshnikov, V. Kulbachinskii, A. Davydov, B. Aronzon, I. Rozhansky, N. Averkiev, K. Kugel, V. Tripathi, Berry phase mechanism of the anomalous hall effect in a disordered two-dimensional magnetic semiconductor structure, Scientific Reports 5 (2015) 17158.
[8] H. Ishizuka, N. Nagaosa, Spin chirality induced skew scattering and anomalous hall effect in chiral magnets, Science Advances 4 (2) (2018) eaap9962.
[9] T. Jungwirth, Q. Niu, A. MacDonald, Anomalous hall effect in ferromagnetic semiconductors, Physical Review Letters 88 (20) (2002), 207208.
[10] R. Yu, W. Zhang, H.-J. Zhang, S.-C. Zhang, X. Dai, Z. Fang, Quantized anomalous hall effect in magnetic topological insulators, Science 329 (5987) (2010) 61–64.
[11] F.D.M. Haldane, Model for a quantum hall effect without landau levels: Condensed-matter realization of the parity anomaly, Physical Review Letters 61 (18) (1988) 2015.
[12] C.-X. Liu, X.-L. Qi, X. Dai, Z. Fang, S.-C. Zhang, Quantum anomalous hall effect in hg 1- y mn y te quantum wells, Physical Review Letters 101 (14) (2008), 146802.
[13] C.-X. Liu, S.-C. Zhang, X.-L. Qi, The quantum anomalous hall effect: Theory and experiment, Annual Review of Condensed Matter Physics 7 (2016) 301–321.
[14] C.-Z. Chang, J. Zhang, X. Feng, J. Shen, Z. Zhang, M. Guo, K. Li, Y. Ou, P. Wei, L.-L. Wang, et al., Experimental observation of the quantum anomalous hall effect in a magnetic topological insulator, Science 340 (6129) (2013) 167–170.
[15] J.-J. Zhu, D.-X. Yao, S.-C. Zhang, K. Chang, Electrically controllable surface magnetism on the surface of topological insulators, Physical Review Letters 106 (9) (2011), 097201.
[16] F. Ye, G.-H. Ding, H. Zhai, Z.-B. Su, Spin helix of magnetic impurities in two-dimensional helical metal, EPL (Europhysics Letters) 90 (4) (2010) 47001.
[17] K. Yasuda, R. Wakatsuki, T. Morimoto, R. Yoshimi, A. Tsukazaki, K. Takahashi, M. Ezawa, M. Kawasaki, N. Nagaosa, Y. Tokura, Geometric hall effects in topological insulator heterostructures, Nature Physics 12 (6) (2016) 555.
[18] C. Liu, Y. Zang, W. Ruan, Y. Gong, K. He, X. Ma, Q.-K. Xue, Y. Wang, Dimensional crossover-induced topological hall effect in a magnetic topological insulator, Physical Review Letters 119 (17) (2017), 176809.
[19] J. Jiang, D. Xiao, F. Wang, J.-H. Shin, D. Andreoli, J. Zhang, R. Xiao, Y.-F. Zhao, M. Kayyalha, L. Zhang, et al., Concurrence of quantum anomalous hall and topological hall effects in magnetic topological insulator sandwich heterostructures, Nature Materials (2020) 1–6.
[20] H. Zhang, C.-X. Liu, X.-L. Qi, X. Dai, Z. Fang, S.-C. Zhang, Topological insulators in bi 2 se 3, bi 2 te 3 and sb 2 te 3 with a single dirac cone on the surface, Nature Physics 5 (6) (2009) 438.
[21] C.-X. Liu, X.-L. Qi, H. Zhang, X. Dai, Z. Fang, S.-C. Zhang, Model hamiltonian for topological insulators, Physical Review B 82 (4) (2010), 045122.
[22] C.-X. Liu, H. Zhang, B. Yan, X.-L. Qi, T. Frauenheim, X. Dai, Z. Fang, S.-C. Zhang, Oscillatory crossover from two-dimensional to three-dimensional topological insulators, Physical Review B 81 (4) (2010), 041307.
[23] Supplementary materials for 'topological hall effect in magnetic topological insulator films'.
[24] P.B. Ndiaye, C.A. Akosa, A. Manchon, Topological hall and spin hall effects in disordered skyrmionic textures, Physical Review B 95 (6) (2017), 064426.

[25] K.-W. Kim, J.-H. Moon, K.-J. Lee, H.-W. Lee, Prediction of giant spin motive force due to rashba spin-orbit coupling, Physical Review Letters 108 (21) (2012), 217202.
[26] W. Koshibae, N. Nagaosa, Theory of antiskyrmions in magnets, Nature Communications 7 (2016) 10542.
[27] S. Datta, Electronic Transport in Mesoscopic Systems, Cambridge University Press, 1997.
[28] P. Bruno, V. Dugaev, M. Taillefumier, Topological hall effect and berry phase in magnetic nanostructures, Physical Review Letters 93 (9) (2004), 096806.
[29] W.-T. Hou, J.-X. Yu, M. Daly, J. Zang, Thermally driven topology in chiral magnets, Physical Review B 96 (14) (2017), 140403.
[30] G. Yin, Y. Liu, Y. Barlas, J. Zang, R.K. Lake, Topological spin hall effect resulting from magnetic skyrmions, Physical Review B 92 (2) (2015), 024411.